Check for updates

ADVANCING EARTH AND SPACE SCIENCES

JGR Solid Earth

RESEARCH ARTICLE

10.1029/2024JB030731

Scattering and Absorption Imaging of the Hengill High-Temperature Geothermal Area, Southwest Iceland

Ferdinando Napolitano[1], Luca De Siena[2], Ortensia Amoroso[1], Thorbjörg Ágústsdóttir[3], Ásdís Benediktsdóttir[4], Mauro Palo[5], Vala Hjörleifsdóttir[6], and Paolo Capuano[1]

[1]Dipartimento di Fisica "E.R. Caianiello", University of Salerno, Fisciano, Italy, [2]Dipartimento di Fisica ed Astronomia "Augusto Righi", Alma Mater Studiorum Bologna, Bologna, Italy, [3]Iceland GeoSurvey (ÍSOR), Kópavogur, Iceland, [4]Reykjavík Energy, Reykjavík, Iceland, [5]Dipartimento di Fisica "Ettore Pancini", Università di Napoli "Federico II", Napoli, Italy, [6]Reykjavík University, Reykjavik, Iceland

Key Points:

- Seismic scattering and absorption imaging are key tools for identifying and mapping geothermal resources
- High-scattering marks the Hengill fissure swarm, low-scattering reveals magmatic intrusions beneath the volcano, acting as a seismic barrier
- Absorption maps indicate a geothermal resource in the non-harnessed Mosfellsheiði area, despite the absence of surface manifestations

Supporting Information:

Supporting Information may be found in the online version of this article.

Correspondence to:

F. Napolitano,
fnapolitano@unisa.it

Citation:

Napolitano, F., De Siena, L., Amoroso, O., Ágústsdóttir, T., Benediktsdóttir, Á., Palo, M., et al. (2025). Scattering and absorption imaging of the Hengill high-temperature geothermal area, southwest Iceland. *Journal of Geophysical Research: Solid Earth*, *130*, e2024JB030731. https://doi.org/10.1029/2024JB030731

Received 8 NOV 2024
Accepted 26 APR 2025

Author Contributions:

Conceptualization: Ferdinando Napolitano, Vala Hjörleifsdóttir, Paolo Capuano
Data curation: Ferdinando Napolitano, Thorbjörg Ágústsdóttir, Ásdís Benediktsdóttir, Vala Hjörleifsdóttir
Formal analysis: Ferdinando Napolitano
Funding acquisition: Paolo Capuano
Investigation: Ferdinando Napolitano, Luca De Siena, Ortensia Amoroso, Thorbjörg Ágústsdóttir, Mauro Palo, Vala Hjörleifsdóttir
Methodology: Ferdinando Napolitano, Luca De Siena
Project administration: Paolo Capuano
Resources: Thorbjörg Ágústsdóttir, Ásdís Benediktsdóttir, Vala Hjörleifsdóttir

© 2025. The Author(s).
This is an open access article under the terms of the Creative Commons Attribution License, which permits use, distribution and reproduction in any medium, provided the original work is properly cited.

Abstract We applied 3D scattering and absorption imaging to the Hengill volcanic area (southwest Iceland), where high-enthalpy geothermal reservoirs are presently harnessed. These techniques have shown the potential for detecting magmatic intrusions and fluid reservoirs in volcanic regions. Here, we target seismic scattering and absorption as proxies of the elastic and anelastic properties of the crust to understand their potential in areas of geothermal energy extraction. The harnessed Nesjavellir geothermal field was used as a benchmark to extend interpretation into non-harnessed areas and provide better insight when evaluating exploitable geo-resources. Shallow, high-scattering anomalies mark the sub-vertical Hengill fissure swarm. Deeper low-scattering volumes likely highlight sub-horizontal magmatic intrusions beneath the Hengill central volcano, whose less fractured volume acts as a barrier for the surrounding seismicity. At Nesjavellir, high absorption co-located with high scattering volumes spatially correlates with previously detected high Vp/Vs volumes, suggesting the existence of fluid- and/or melt-filled complex seismically active networks of faults and fractures. Our results suggest the presence of geothermal reservoirs in non-harnessed areas (Mosfellsheiði and Ölkelduháls) shown by similar high-absorption anomalies at depths comparable with the Nesjavellir geothermal resource. Scattering and absorption imaging complement more standard imaging techniques, improving interpretation in geothermal resource exploration.

Plain Language Summary We conducted 3D imaging of scattering and absorption of seismic waves to study the Hengill volcanic area in Iceland, with the goal of identifying potential underground magma and/or fluid reservoirs that are critical for geothermal energy. While scattering is highly sensitive to the presence of faults and fractures in the medium, absorption is more responsive to fluids, magma, and high-temperature rocks. This work aims to jointly interpret our images with previous geological and geophysical evidence to find potential geothermal resources, using the extensively studied Nesjavellir geothermal field as a reference. Our findings suggest that similar geothermal reservoirs may exist in nearby non-harnessed areas. The study highlights the value of these imaging techniques for exploring new geothermal energy sources.

1. Introduction

The Hengill central volcano is located in the southwestern part of Iceland, about 30 km east of the capital Reykjavík, at a triple junction formed by the Reykjanes Peninsula (RP), the Western Volcanic Zone (WVZ) and the South Iceland Seismic Zone (SISZ) (Einarsson, 2008). This region is geologically characterized by alternating hyaloclastite layers and fractured basalt deposits formed as a consequence of alternating sub-glacial and subaerial volcanic eruptions, ranging from 0.12 Myr to 2,000 years (Sæmundsson et al., 2016). Hyaloclastites have formed ridge-shaped mountains and tuyas, such as Mt. Hengill (803 m a.s.l.). Hengill is the youngest volcanic system in the Hengill volcanic area, intersected by fissures and normal faults striking N30°E and extending northwards to Lake Þingvallavatn (Figure 1a). This region also comprises minor shield volcanoes on the edges of the Hengill fissure swarm, such as Mosfellsheiði. Hengill volcano last erupted about 1800 years ago (Sinton et al., 2005). Directly east of the Hengill volcanic system lies the Hrómundartindur (540 m a.s.l.) system, which last erupted approximately 11,000 years ago (Sæmundsson et al., 2016). The oldest of the three volcanic systems in the Hengill region is Grensdalur (497 m a.s.l). It is located farthest to the southeast, was last active during the Pleistocene (Figure 1a), and is considered extinct.

Software: Ferdinando Napolitano, Luca De Siena
Supervision: Luca De Siena, Ortensia Amoroso, Vala Hjörleifsdóttir, Paolo Capuano
Validation: Ferdinando Napolitano, Luca De Siena, Ortensia Amoroso, Thorbjörg Ágústsdóttir, Ásdís Benediktsdóttir
Visualization: Ortensia Amoroso
Writing – review & editing: Ferdinando Napolitano, Luca De Siena, Ortensia Amoroso, Thorbjörg Ágústsdóttir, Ásdís Benediktsdóttir, Mauro Palo, Vala Hjörleifsdóttir, Paolo Capuano

The two largest geothermal power plants in Iceland are located in the Hengill volcanic area. The southern Hellisheiði, and the northern Nesjavellir power plants (Figure 1a), are operated by ON Power and situated in areas where geothermal fluids migrate through fractures and fissures within the porous basaltic crust. According to Gunnarsson and Aradóttir (2015), the reservoir temperature in the Hengill region varies between 200°C and 340°C. The energy is used for the production of electricity, space heating in Reykjavík and the surrounding towns, and other direct applications. 23 production wells are currently in use in the Nesjavellir geothermal field and 49 in Hellisheiði. After passing through the power plant, the geothermal fluid is reinjected into both shallow (a few hundred meters deep) and deep injection wells (>1,800 m deep).

Seismicity occurring in clusters characterizes the Hengill region, with natural seismicity linked to volcanic, tectonic, geothermal and anthropogenic activity (Bodvarsson et al., 1996; Brandsdóttir et al., 2010; Li et al., 2019; Obermann et al., 2022; Rögnvaldsson et al., 1996). Earthquake depths are mainly confined to the uppermost 6–7 km of the crust, which is used to infer the depth of the brittle-ductile transition (Li et al., 2019; Tryggvason et al., 2002). The highly variable volcanic structure under the Hrómundartindur and Grensdalur volcanic systems is likely composed of kilometers-long solidified magmatic intrusions that reach depths of around 3–5 km (Árnason et al., 2010; Franzson et al., 2010). Just south of Hrómundartindur, uplift events were observed between 1993 and 1999, and again in 2017–2018, causing intense seismicity across the whole Hengill region (Ducrocq et al., 2021; Jakobsdóttir, 2008; Sigmundsson et al., 1997). Models propose that the source of the uplift was a pressure source of either a magmatic or hydrothermal origin at depths of 6–7 km, thus deeper than previously reported solidified magma formations (Ducrocq et al., 2021; Feigl et al., 2000; Sigmundsson et al., 1997). Local earthquake tomography studies (Foulger & Toomey, 1989; Jousset et al., 2011; Tryggvason et al., 2002) show positive P- and S-wave velocity anomalies and low Vp/Vs ratios beneath the central volcanoes in the shallowest two km depth, which have been interpreted as solidified magmatic intrusions. Near the surface, high Vp and low Vp/Vs have been correlated with steam, hot springs and other geothermal manifestations. At depths of 4–10 km below Hengill volcano, Tryggvason et al. (2002) found low P- and S-wave velocity anomalies, interpreted as supercritical fluid, meteoric water and fluids of magmatic origin filling fractured volcanic fissures, with no partial melt.

More recently, denser networks of temporary seismic stations were deployed in the Hengill region as a part of the H2020 project Science for Clean Energy (S4CE) and the Geothermica-funded project COntrol SEISmicity and Manage Induced earthQuakes (COSEISMIQ). The increased number of detected earthquakes allowed more detailed travel-time tomographies (Amoroso et al., 2022; Obermann et al., 2022; Wu et al., 2024) and a new shear-wave velocity model (Sanchez-Pastor et al., 2021) that used larger data sets together with new methods. The first study focuses on the northern part of the Hengill volcanic field, around the Nesjavellir power plant, whereas the other two encompass the entire volcanic field. In these studies, low-Vp/Vs anomalies marked the steam-dominated production area, where seismicity appears scattered rather than focused on well-delineated faults. High Vp/Vs ratios at depth, on the other hand, likely reflect magmatic intrusions near the brittle-ductile zone, possibly feeding the geothermal systems. These interpretations were further supported by comparison with transient electromagnetic (TEM) and magnetotelluric (MT) measurements derived from Árnason et al. (2010) and Vilhjálmsson et al. (2019). The comparisons showed a strong spatial correlation between high (/low) resistivity and low (/high) Vp/Vs, consistent with the general understanding that fluid-rich, highly fractured zones exhibit both low resistivity and high Vp/Vs, while more consolidated or vapor-dominated regions tend to show high resistivity and low Vp/Vs. This highlights the importance of integrating multiple geophysical methods to fully characterize geothermal reservoirs. In the context of such a wide range of analyses, attenuation studies are missing.

Seismic attenuation is primarily due to two physical mechanisms: seismic scattering and absorption (Sato et al., 2012). Measurements of these parameters are reliable proxies for the spatial extension of faults and fluid reservoirs across tectonic, volcanic and hydrothermal settings (De Siena et al., 2016; Di Martino, De Siena, Serlenga, et al., 2022; Gabrielli et al., 2022, 2023; Napolitano et al., 2020, 2023; Reiss et al., 2022). Scattering is a measure of heterogeneity within the crust (Takahashi et al., 2007); increased heterogeneity within the medium (e.g., fault networks) enhances wave trapping that increases energy across the earthquake coda, marking tectonic interactions and lithological contrasts (Gabrielli et al., 2022, 2023; Napolitano et al., 2023). Seismic absorption is mostly sensitive to magma and fluid reservoirs, strain rate and pore space topology within the crust (Guardo et al., 2022; Napolitano et al., 2023; Reiss et al., 2022; Talone et al., 2023).

21699356, 2025, 5, Downloaded from https://agupubs.onlinelibrary.wiley.com/doi/10.1029/2024JB030731 by CochraneItalia, Wiley Online Library on [09/05/2025]. See the Terms and Conditions (https://onlinelibrary.wiley.com/terms-and-conditions) on Wiley Online Library for rules of use; OA articles are governed by the applicable Creative Commons License

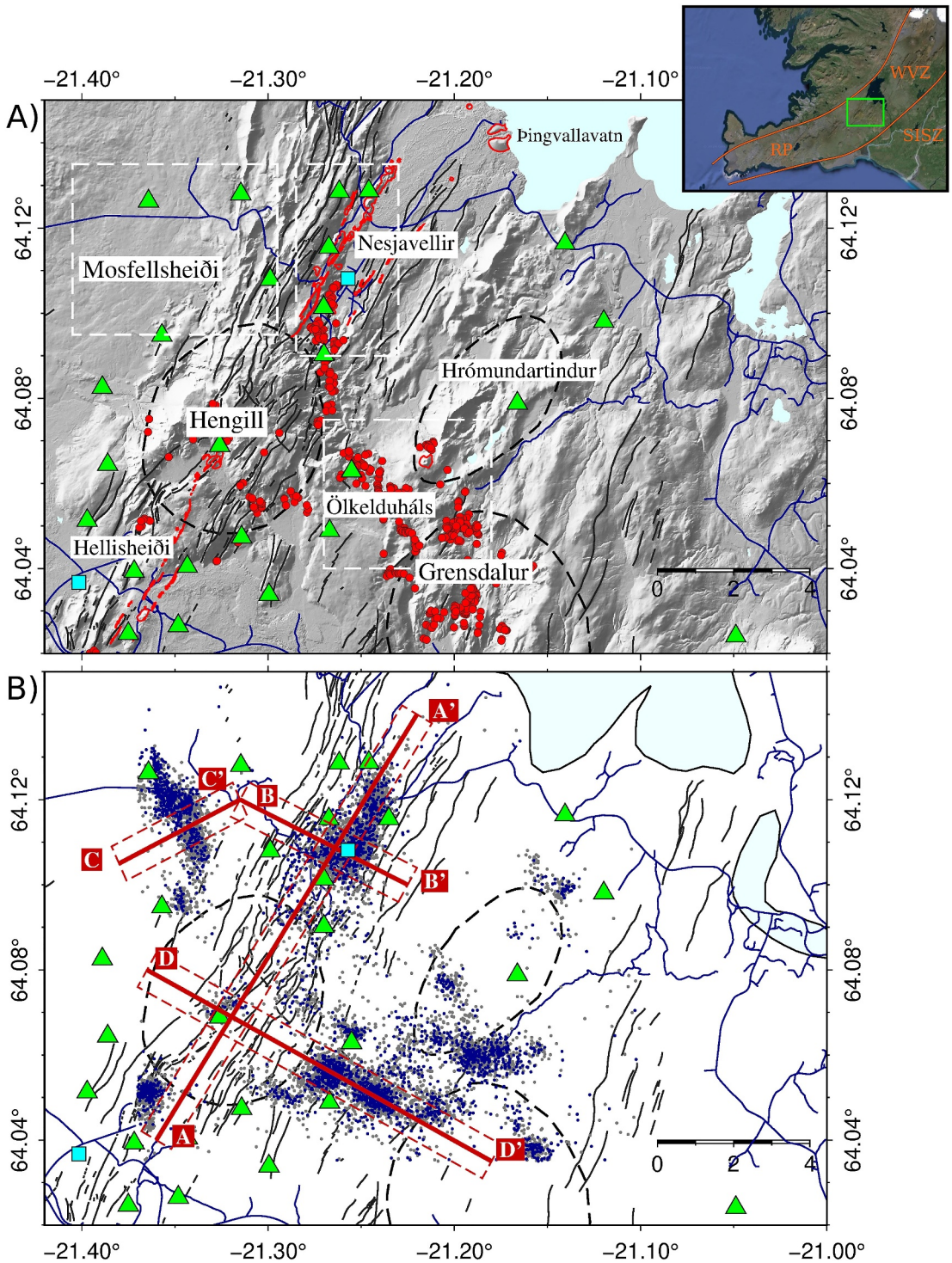

Figure 1. The Hengill volcanic region. Both panels show fissures and faults as black thin lines (Sæmundsson et al., 2016), roads as thick blue lines, seismic stations as green triangles, the Nesjavellir and Hellisheiði power plant locations with cyan squares. Black dashed lines contour volcanic edifices (Árnason et al., 1986). (a): Place names are labeled. Red circles are the fumaroles and red thin lines are the eruptive fissures and craters. The three white dashed rectangles highlight the Nesjavellir, Mosfellsheiði and Ölkelduháls regions. The inset map shows the location of the study area in the Iceland framework. Orange lines are the plate boundaries, green rectangle is the study area of this paper. Labels: RP: Reykjanes Peninsula (RP), the Western Volcanic Zone (WVZ) and the South Iceland Seismic Zone (SISZ). (b): gray and blue dots are earthquake locations of the starting and final selected data set (occurred between 2017 and 2022) provided by Icelandic GeoSurvey (ÍSOR), respectively. Dark red lines mark cross-sections AA', BB', CC' and DD' (dashed lines show their 0.5 km width) (used to interpret the results along and perpendicular to the main geological trend).

21699356, 2025, 5, Downloaded from https://agupubs.onlinelibrary.wiley.com/doi/10.1029/2024JB030731 by CochraneItalia, Wiley Online Library on [09/05/2025]. See the Terms and Conditions (https://onlinelibrary.wiley.com/terms-and-conditions) on Wiley Online Library for rules of use; OA articles are governed by the applicable Creative Commons License

The separation of scattering and absorption contribution through peak delay and coda decay is becoming a standard combination in seismology, given their sensitivity to different structures and processes within the same volume. Peak delay is defined as the time lag between the S-wave onset and the highest amplitude reached by the seismogram envelope (Takahashi et al., 2007), interpreted as a proxy for forward scattering within the lithosphere. The inverse coda quality factor (Q_c^{-1}) is a measure of the decay of coda energy with lapse time from the earthquake origin time. It is a measurement of seismic absorption of the medium (Q_i^{-1}, i.e., $Q_c \approx Q_i$—Aki & Chouet, 1975; Calvet & Margerin, 2013; Shapiro et al., 2000) in the diffusion regime. This condition is fulfilled when (a) the beginning of the coda wave window is taken late enough into the seismogram for diffusion to be reached and (b) no coda wave energy is lost through leakage into the mantle, nor are coherent phases included in the coda window (Margerin, 2017). These scattering and absorption proxies have been recently calibrated in the laboratory and at smaller Earth scales. King, De Siena, Benson, and Vinciguerra (2023), King, De Siena, Zhang, et al. (2023) showed that trapped and resonant waves drastically increase peak delays at a boundary, making it a marker of strain increase and fracturing (high peak delays), and overpressure in the pore space (low peak delays). Di Martino, De Siena, Serlenga, et al. (2022), Di Martino, De Siena, and Tisato (2022) demonstrated that the heterogeneity of an undeformed synthetic sample, mimicking a volcanic basaltic rock, is sufficient to change the intermediate coda drastically. Still, the authors demonstrate that in absorption imaging the late lapse time coda decay remains a function of fluid saturation (in their sample case, air, in its pore space) and pore space topology.

The combined use of these techniques has identified intrusions in mountain chains (Calvet et al., 2013) and magmatic systems (De Siena et al., 2016; Guardo et al., 2022; Reiss et al., 2022) as high scattering and high absorption anomalies. In active tectonic settings, high scattering and high absorption anomalies has been interpreted as overpressurized fluids in a highly fractured medium, such as the Mt. Pollino area (Southern Italy) that hosted a 4-year long swarm-like sequence (Napolitano et al., 2023). High Vp/Vs ratio and pore fluid pressure with values reaching 35 MPa in the same crustal volume corroborated this interpretation (De Matteis et al., 2021; Napolitano et al., 2021). Similar findings for the 2016–2017 central Italy sequence linked thrust faults and pore pressure to seismic activity (Gabrielli et al., 2022). In the Natron Rift (Northern Tanzania), scattering revealed fractures and deep fluid-filled faults channeling carbonatites to Ol Doinyo Lengai eruptions, with high-absorption anomalies mapping sills, dikes, and fluid reservoirs (Reiss et al., 2022). At Deception Island (Antarctica), high-absorption anomalies identified intrusions linked to caldera eruptions (Guardo et al., 2022). In Campi Flegrei (Southern Italy), near-surface scattering exposed faults separating hydrothermal plumes from CO2-rich zones, while absorption anomalies distinguished between liquid- and vapor-rich fluids (Di Martino, De Siena, Serlenga, et al., 2022).

In this study, scattering and absorption imaging techniques are, for the first time, applied to a high-enthalpy geothermal area. We aim to better understand the physical elastic and anelastic properties of the crust in areas of geothermal utilization. Using as a benchmark the harnessed Nesjavellir geothermal field, where extensive geological, geophysical and well-log information is available, we also analyzed two non-harnessed areas (Ölkelduháls and Mosfellsheiði, Figure 1a), suggesting the existence of similar exploitable fluids reservoirs.

2. Data Collection and Preprocessing

Refined locations of 10,191 seismic events (gray dots in Figure 1b) were provided by Iceland GeoSurvey (ÍSOR) on behalf of Reykjavík Energy/ON Power. The events, located between lat: 64.02°N–64.15°N and lon: 21.1°W–21.4°W, range from local magnitudes M_L-0.6 and M_L 3.9, with a maximum depth of 9.7 km. The events were recorded between January 2017 and December 2022 by permanent and temporary seismic stations operated by four seismic networks: ON-ÍSOR operated by Iceland GeoSurvey for ON Power and Carbfix, two stations funded through the H2020 funded S4CE project, Icelandic National Digital Seismograph Network (SIL), and the Geothermica funded COSEISMIQ network. For our analysis, we used earthquakes recorded on a subset of 24 seismic stations that were located within the target area (Figure 1).

We defined selection criteria for earthquakes from the initial data set, setting a minimum local magnitude (M_L) threshold of 0.5 and retaining only the E-W component with both P- and S-phase picking available. We applied a declustering procedure (Reiss et al., 2022) with the goal of reducing earthquake oversampling due to clustering of seismicity while removing the most unstable measurements in terms of signal-to-noise ratio, for which the lower threshold has been fixed to 3. In practice, we first divided the study region in blocks of length 1 km in all three directions; we then divided each of these volumes into sub-volumes by splitting each side of the cube into five

21699356, 2025, 5, Downloaded from https://agupubs.onlinelibrary.wiley.com/doi/10.1029/2024JB030731 by CochraneItalia, Wiley Online Library on [09/05/2025]. See the Terms and Conditions (https://onlinelibrary.wiley.com/terms-and-conditions) on Wiley Online Library for rules of use; OA articles are governed by the applicable Creative Commons License

segments; we finally retained only those event-station pairs with the lowest uncertainty on coda-decay measurement in each sub-volume. The final data set, input for the following analyses, consists of around 10,600 waveforms, belonging to 2240 earthquakes. The waveforms have been filtered with a 8–16 Hz (central frequency, $f_c = 12$ Hz), 4-th order, zero-phase, Butterworth band-pass filter. This frequency band contains the largest portion of the energy produced by such small-magnitude earthquakes while ensuring a prevalence of body waves within the coda and no contamination due to the strong microseism in Iceland. The envelopes were computed using a Hilbert transform and subsequently smoothed with a moving window duration $t = 8/f_c$.

3. Methods

The analyses have been performed using Murat3.0, the third release of an open-access code (De Siena et al., 2014) that enables the measurement and 3D modeling of spatial variations in total attenuation, scattering, and absorption. The code, over the past 10 years, has been widely applied in different tectonic (Borleanu et al., 2017; Gabrielli et al., 2022, 2023; Napolitano et al., 2020, 2023) and volcanic (Di Martino, De Siena, Serlenga, et al., 2022; Reiss et al., 2022) contexts. The methods used for producing scattering, absorption imaging and clustering analysis are described in the following subsections.

3.1. Peak Delay Method

A clear indication of the contribution of scattering to the attenuation of seismic waves can be observed in the delay between the onset of S-waves and the time of maximum amplitude in the envelope, referred to as *peak-delay time*. This delay widens as the distance between the seismic source and the receiver increases (Calvet et al., 2013; Takahashi et al., 2007). The logarithmic increase in peak delay times (t^{pd}, measured in seconds) exhibits a linear relationship with the logarithm of the hypocentral distance (R_H, measured in km), expressed by the equation:

$$\log_{10} t^{pd}(f) = A(f) + B(f) \cdot \log_{10} R_H \tag{1}$$

here, $A(f)$ and $B(f)$ are the coefficients obtained from regression fit (Gusev & Abubakirov, 1999). The hypocentral distance is computed using a 1D velocity model specific for the Nesjavellir area (Amoroso et al., 2022), allowing the rays to propagate in a 3D grid with a ray-bending approach (De Siena et al., 2017, from Block, 1991). The amount of scattering along the ray path is determined by comparing the calculated peak delay time of the ith waveform (t_i^{pd} in Equation 2, gray circles in Figure S1 in Supporting Information S1) to the theoretical peak delay at the corresponding hypocentral distance (t^{pd} in Equation 2, red line in Figure S1 in Supporting Information S1):

$$\Delta \log_{10} t(f) = \log_{10}\left[t_i^{pd}(f)\right] - \log_{10}\left[t^{pd}(f)\right] \tag{2}$$

Positive or negative variations compared to the average value measured with the linear trend identify high- and low-scattering areas. Positive variations are associated with heterogeneous crustal regions, while negative variations with solid and compact volumes. Figure S1 in Supporting Information S1 shows the log-log plot of peak delays within one standard deviation from the linear fit as a function of S-wave travel time for the Nesjavellir area at a central frequency of 12 Hz.

For each source-receiver ray, the peak delay time is computed as the time lag between the S-wave onset and the maximum S-wave amplitude (Takahashi et al., 2007). The logarithmic variation of the S-wave peak delay time is then mapped, assuming source-receiver sensitivity on rays and employing a conventional weighted regionalization technique (Calvet et al., 2013; Gabrielli et al., 2023) on a grid with 1 km vertically spaced nodes in all three directions. The stability of peak delay analysis is assessed by computing the hit count maps at different depths (Figure S2 in Supporting Information S1), considering peak delay variations within blocks crossed by at least 20 seismic rays.

3.2. Q-Coda Method

Different methods have been developed to assess strong lateral variations in lithospheric characteristics using coda wave attenuation. These methods share a common initial step of computing the energy density envelopes of coda waves to determine the coda quality factor (Qc). The energy within the coda window ($E(t, f)$) at lapse-time t and frequency f is:

21699356, 2025, 5, Downloaded from https://agupubs.onlinelibrary.wiley.com/doi/10.1029/2024JB030731 by CochraneItalia, Wiley Online Library on [09/05/2025]. See the Terms and Conditions (https://onlinelibrary.wiley.com/terms-and-conditions) on Wiley Online Library for rules of use; OA articles are governed by the applicable Creative Commons License

$$E(t,f) = S(f)\, t^{-\alpha} \exp\left(-2\pi f t Q_c^{-1}(f)\right) \tag{3}$$

where $S(f)$ is the source term, t is expressed in seconds between the origin time of the event and the beginning of the coda window, and the constant α is related to geometrical spreading and fixed to 3/2 in a multiple scattering interpretation (Calvet et al., 2013). The algorithm MuRAT3D employs a linearized approach to solve this equation, proven to be computationally faster than a grid search and equivalent to the linearized approach (Napolitano et al., 2020):

$$\frac{\ln[E(t,f)\cdot t^{\alpha}]}{2\pi f} = \frac{\ln[S(f)]}{2\pi f} - Q_c{}^{-1} t \tag{4}$$

In volcanic media like those under study, the onset of diffusion is observed immediately after the S-wave arrival when using active sources (Prudencio et al., 2017; Wegler, 2004). When using earthquakes, this onset ranges from a few seconds from the S-wave arrival for very-shallow shallow seismicity (De Siena et al., 2013) to tens of seconds after the S-wave arrival for deeper earthquakes and depending on frequency and topography (De Siena et al., 2016; Gabrielli et al., 2020). We set both lapse time and coda window length to 10 s for the entire data set, which is a reasonable choice to reach equipartition with a very local data set and shallow earthquakes (above 7 km depth, as discussed in Napolitano et al., 2020). We also tested the stability of $Q_c{}^{-1}$ measurements computed for each waveform as a function of the ray length (Calvet et al., 2013) and of the earthquake index at a central frequency of 12 Hz (upper panels in Figure S3 in Supporting Information S1). To better visualize these results, we computed a moving average and standard deviation of $Q_c{}^{-1}$ on a 500-point window, showing a clear constant $Q_c{}^{-1}$ value around 0.002 within the selected ray length range at 12 Hz (lower panels in Figure S3 in Supporting Information S1).

Seismic absorption tomography (Sketsiou et al., 2020) uses an inversion scheme (De Siena et al., 2017) based on 3D diffusive sensitivity kernels (Del Pezzo et al., 2018; Mayor et al., 2016; Obermann et al., 2013; Ogiso, 2019), which in turn are based on Paasschen's equations (Paasschen, 1997) and are independent of the 3D velocity model choice. To compute the sensitivity kernel, we set two fundamental quantities: seismic albedo and extinction length. The seismic albedo is the dimensionless ratio of the scattering loss to total attenuation. The extinction length is the distance in km over which the primary S-wave energy is decreased by e^{-1}. They are set to average values for similar geothermal regions, specifically the Campi Flegrei caldera (Akande et al., 2019). The sensitivity kernels require constant S-wave velocities in the computation, which has been set to 3.0 km/s, obtained as the average value from the 3D velocity model for the Nesjavellir area (Amoroso et al., 2022). We set the same grid defined for peak delay (1-km spaced nodes along the three directions of motion). The spatial variation maps of $Q_c{}^{-1}$ are validated through checkerboard tests at a depth of 4.3 km, where all the high-attenuation anomalies discussed have been located (Figure S4 in Supporting Information S1). The synthetic test allows us to interpret 2-km wide anomalies in the three directions of motion.

3.3. Earthquake Clustering

Clusters of similar earthquakes suggest the presence of highly attenuating bodies (fluids, melt, high temperature rocks) permeating the highly fractured seismogenic volume, a phenomenon observed across various geological contexts, such as subduction zones, mountain ranges, volcanic, and geothermal areas (Danrè et al., 2022; De Barros et al., 2020; Fisher et al., 2014; Napolitano et al., 2021; Palo, Ogliari, & Sakwa, 2024; Palo, Scotto di Uccio, Picozzi, & Festa, 2024; Ross et al., 2020; Ruhl et al., 2016).

In the study area, clusters of similar earthquakes have been defined following the approach described in Palo et al. (2023). In this approach, a similarity coefficient ranging between 0 and 1 is defined for each pair of events in the catalog. The similarity between pairs of earthquakes was here measured as the largest cross-correlation (CC) between the P-wave phases (in a time window of 1 s starting 0.2 s before the P-wave arrival time) among the stations that have detected the events of the pair. We used the vertical components of the waveforms belonging to the same data set used to perform the attenuation tomography. A 4-th order Butterworth frequency filter in the 1–20 Hz frequency band was applied beforehand.

21699356, 2025, 5, Downloaded from https://agupubs.onlinelibrary.wiley.com/doi/10.1029/2024JB030731 by CochraneItalia, Wiley Online Library on [09/05/2025]. See the Terms and Conditions (https://onlinelibrary.wiley.com/terms-and-conditions) on Wiley Online Library for rules of use; OA articles are governed by the applicable Creative Commons License

This method estimates the similarity between earthquakes even when no station has recorded both events. It relies on hierarchical agglomerative clustering (HAC) applied to the CC matrix at each station, grouping earthquakes with similar waveforms into one-station clusters. Consider a case where event 1 is detected only at station A and event 2 only at station B. Since no direct comparison is possible, the algorithm leverages other earthquakes that belong to their respective one-station clusters: U1A (earthquakes similar to event 1 at station A) and U2B (earthquakes similar to event 2 at station B). The key idea is to identify earthquakes from U1A that were also recorded at station B and earthquakes from U2B that were recorded at station A. These serve as "bridges" between the two stations, allowing indirect similarity estimation. Cross-correlations are computed between event 1 and the earthquakes in U2B, as well as between event 2 and the earthquakes in U1A. These values are then averaged to provide a similarity estimate for the event pair. Eventually, a similarity coefficient is assigned to all earthquake pairs thus defining a multi-channel similarity matrix (MCM). HAC applied to MCM provides finally a multi-channel cluster index to all catalog events. For further technical details, see Palo et al. (2023).

Only absolute clusters whose mean CC (averaged over stations and earthquake pairs) was equal to or larger than 0.7 were selected and displayed here.

4. Results and Discussion

In Figures 2 and 3, we show the horizontal depth slices and a zoom-in of the Nesjavellir production area at 4.3 km, slicing the 3D peak delay (scattering parameter, as defined in Section 3) and Q_c^{-1} (absorption parameter, as defined in Section 3) models of the Hengill geothermal area for a central frequency of 12 Hz. In each map, we show earthquakes with magnitude M_L greater than or equal to 0.5, whose depths are ±1 km from each slice. Scattering maps (left panels) show positive (red) or negative (blue) anomalies relative to the average peak delay value at a certain hypocentral distance. Blocks crossed by less than 20 rays are masked, as shown by the hit count map (Figure S2 in Supporting Information S1). The Nesjavellir (Ne) field and the Hengill central volcano (He) are the best-recovered areas at depths of 1–7.6 km, while the entire study region is well-recovered between 3 and 7.6 km depth. Absorption maps (Q_c^{-1}, right panels) show higher values (up to 0.013) using brighter colors. Checkerboard tests (Figure S4 in Supporting Information S1) allow us to interpret the most significant high-absorption anomalies. Well-resolved Qc^{-1} areas are contoured by thin white dashed lines. The chosen grid spacing for regionalization (peak delay) and inversion (Q_c^{-1}) allows us to interpret 1-km wide anomalies. The declustering procedure (Reiss et al., 2022) mitigates the effect of spatially colocated seismicity on the scattering and absorption models.

In the following sections, seismic scattering and absorption anomalies are discussed in light of the most recent geophysical literature on the Hengill geothermal area. We have split the discussion into three subsections: the Hengill central volcano (He), the Nesjavellir geothermal field (Ne), and the two non-harnessed geothermal areas (Mosfellsheiði and Ölkelduháls). The last three areas have been marked by white dashed rectangles in Figure 1, while the Hengill central volcano is already contoured by a black dashed line.

4.1. Hengill Central Volcano (He)

Scattering is well resolved between 1.1 and 6.5 km depth (Figure S2 in Supporting Information S1), however, as indicated by the checkerboard tests, resolution is too poor to interpret absorption anomalies at any depth below the volcano (Figure S4 in Supporting Information S1). In this section, we will thus focus on and interpret only the scattering results. This discrepancy in the resolution of scattering and absorption arises from the differences in sensitivity, together with the distribution of seismicity, which is clustered and predominantly located outside or around the Hengill central volcano (Figure 1). The sensitivity differences emerge as the scattering attributes are mapped using high-frequency rays, while absorption attributes utilize diffusive sensitivity kernels with maxima near sources and receivers. In the case of Hengill, there is only one seismic station within the central volcano, and the seismicity is sparse (Figure 1).

Peak delay maps at 1.1 and 2.2 km (Figure 2) show a SW-NE-trending high-scattering anomaly crossing Hengill. The SW-NE orientation and its shallow depth correlate well with the SW-NE trending Hengill fissure swarm that transects the central volcano (as is common in Iceland). This is especially true for the western part of the fissure swarm, whereas a low-scattering anomaly dominates the eastern part. The area immediately outside the surface trace of the Hengill central volcano is marked by low-scattering anomalies to the west and east, whereas high scattering anomalies dominate north and south of it. The high-to-low scattering contrasts on the west and east side

21699356, 2025, 5, Downloaded from https://agupubs.onlinelibrary.wiley.com/doi/10.1029/2024JB030731 by CochraneItalia, Wiley Online Library on [09/05/2025]. See the Terms and Conditions (https://onlinelibrary.wiley.com/terms-and-conditions) on Wiley Online Library for rules of use; OA articles are governed by the applicable Creative Commons License

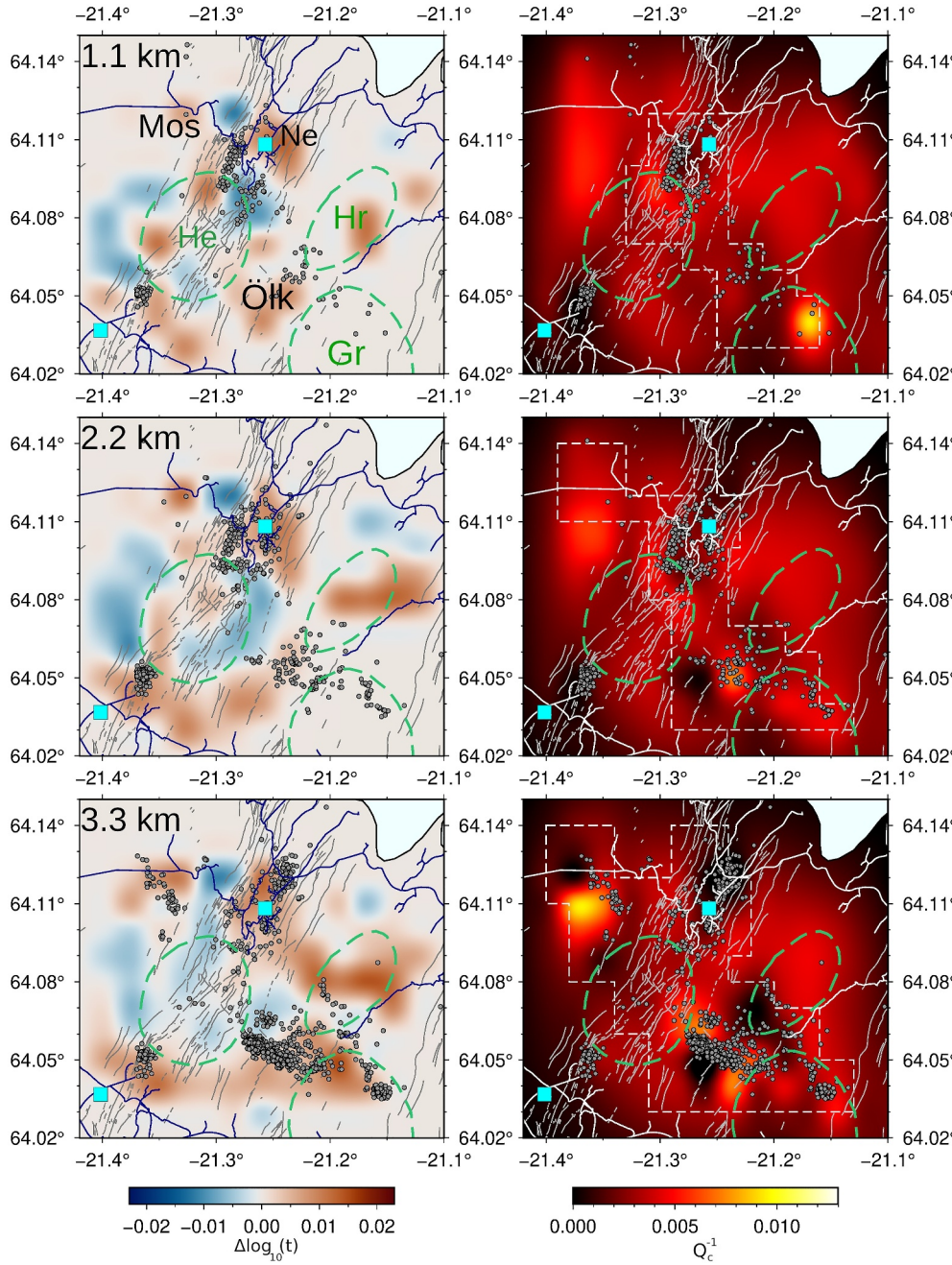

Figure 2. Peak delay (left panels) and Q_c^{-1} (right panels) horizontal cross-sections through the model obtained at 3 different depths for f_c = 12 Hz in the Hengill area. Dark gray dots show seismic events within 1 km from the cross-section depth. The contour of the surface trace of the three central volcanoes (Figure 1) are marked by green dashed lines (He—Hengill, Gr—Grensdalur, Hr—Hrómundartindur). Light gray lines, blue/white lines, and cyan squares show faults and fissure swarms, roads, and the Nesjavellir and Hellisheiði power plants, respectively. Peak delay variations are shown only when more than 20 rays cross the parameter space block (hit count in Figure S2 in Supporting Information S1). Well-resolved areas of Q_c^{-1} (checkerboard test in Figure S4 in Supporting Information S1) are contoured by thin white dashed lines.

of the Hengill central volcano reflects its surface trace, especially at 2.2 km depth, which can be a sign of the heterogeneity in the fault/fracture orientation caused by the complex interplay between tectonic forces (i.e., divergent deformation from rifting) and magmatic or hydrothermal activities.

21699356, 2025, 5, Downloaded from https://agupubs.onlinelibrary.wiley.com/doi/10.1029/2024JB030731 by CochraneItalia, Wiley Online Library on [09/05/2025]. See the Terms and Conditions (https://onlinelibrary.wiley.com/terms-and-conditions) on Wiley Online Library for rules of use; OA articles are governed by the applicable Creative Commons License

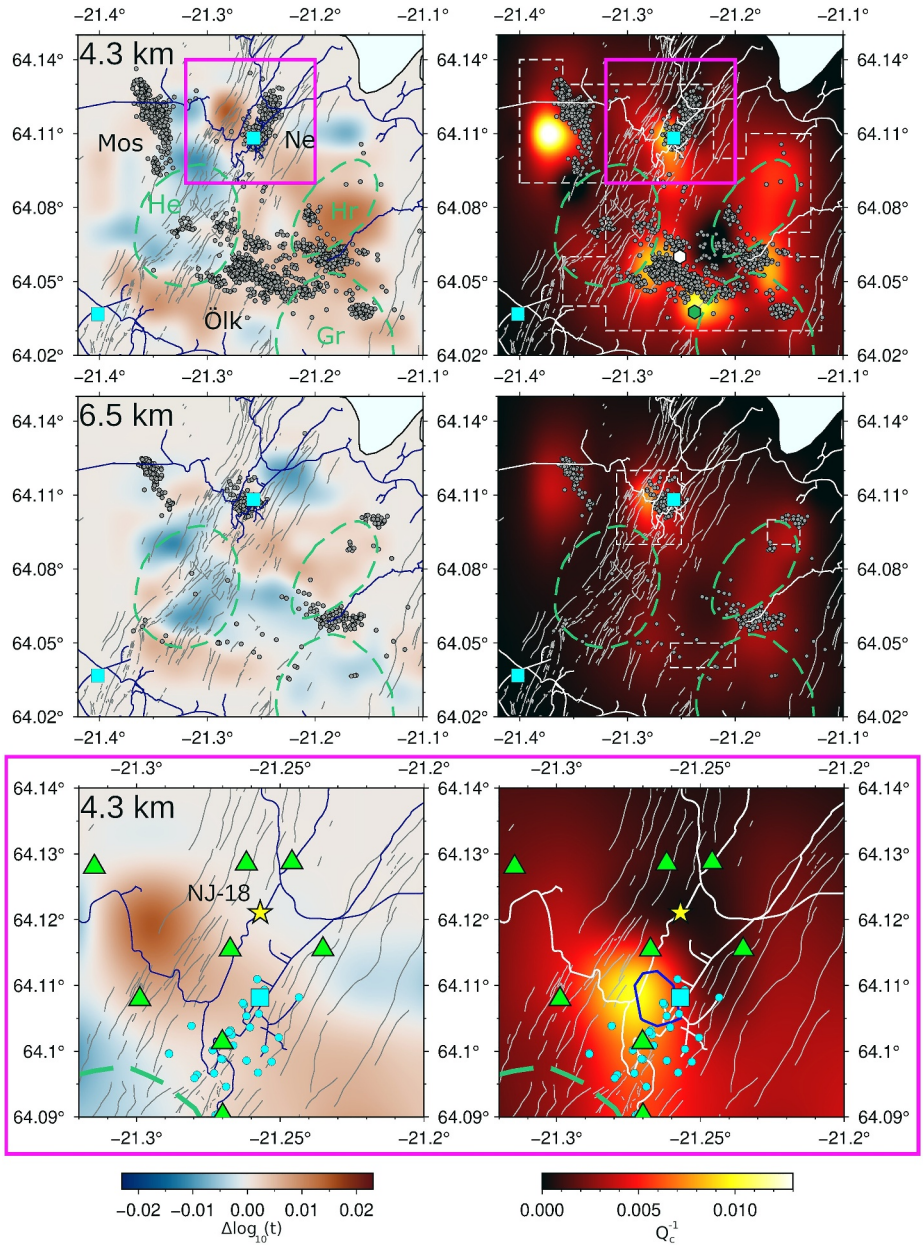

Figure 3. Peak delay (left panels) and Q_c^{-1} (right panels) horizontal cross-sections through the model obtained at 4.3 and 6.5 km depth for $f_c = 12$ Hz in the Hengill area. Dark gray dots show seismic events within 1 km from the cross-section depth. The contour of the surface trace of the three central volcanoes (Figure 1) are marked by green dashed lines (He—Hengill, Gr—Grensdalur, Hr—Hrómundartindur). Light gray lines, blue/white lines, and cyan squares show faults and fissure swarms, roads, and the Nesjavellir and Hellisheiði power plants, respectively. Well-resolved areas of Q_c^{-1} (checkerboard test in Figure S4 in Supporting Information S1) are contoured by thin white dashed lines. White hexagon at 4.3 km depth is the center of the 2006–2017 subsidence (Juncu et al., 2017) and the green hexagon is the center of the 1993–1999 uplift episode (Feigl et al., 2000). Magenta box: Zoom-in on the scattering and absorption anomalies under the Nesjavellir (Ne) area, at 4.3 km depth. Green triangles show the locations of the seismic stations, Nesjavellir power plant and production wells are shown with cyan square and circles, respectively. The location of NJ-18, the only deep injection well at the time of this study is the yellow star. The blue line in the absorption image represents the Vp/Vs = 1.9 isoline obtained from seismic tomography (Amoroso et al., 2022).

At 3 km depth, the scattering patterns change. The shallow "ring-shaped" low-scattering anomaly following the volcano contour becomes a single low-scattering anomaly, reaching down to 7 km depth (Figures 2 and 3, slice AA' in Figure 4). The anisotropic model by Wu et al. (2024) observed a change at the same depth. Shallow sub-

21699356, 2025, 5, Downloaded from https://agupubs.onlinelibrary.wiley.com/doi/10.1029/2024JB030731 by CochraneItalia, Wiley Online Library on [09/05/2025]. See the Terms and Conditions (https://onlinelibrary.wiley.com/terms-and-conditions) on Wiley Online Library for rules of use; OA articles are governed by the applicable Creative Commons License

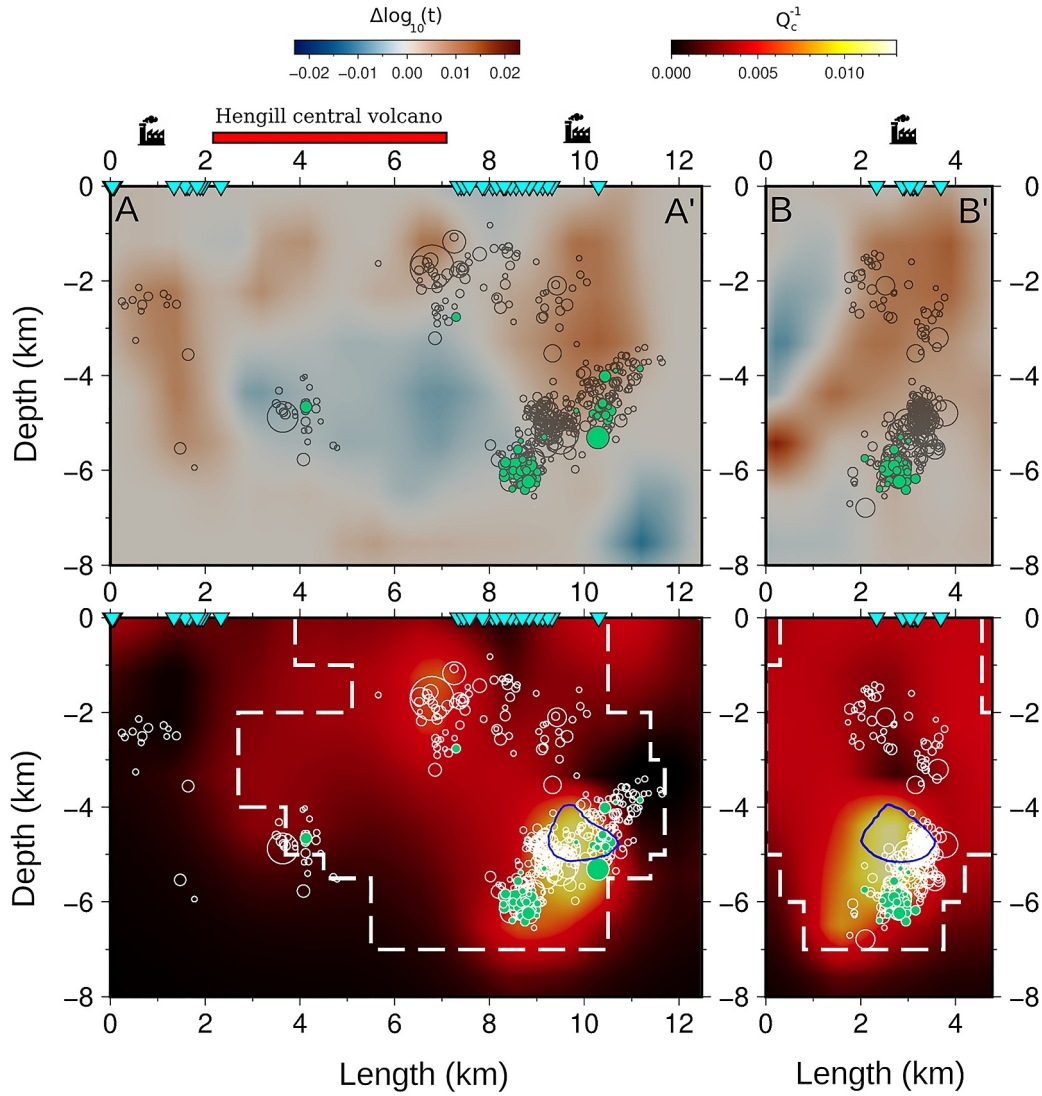

Figure 4. Cross-sections AA' and BB' (see Figure 1b for reference) showing scattering (upper panels) and absorption (lower panels) results. The blue line represents the Vp/Vs = 1.9 contour obtained from seismic tomography (Amoroso et al., 2022). Gray and white circles show the earthquakes within 500 m from each cross-section. The green circles belong to clusters of events producing similar waveforms. The trace of the Hengill central volcano on the cross-section is shown with a red bar. Well heads in the Hellisheiði (left of Hengill central volcano) and Nesjavellir (right of Hengill central volcano) production wells are shown as magenta triangles. Hellisheiði (left) and Nesjavellir (right) power plant locations are shown with small black industry symbols. Well-resolved absorption models defined by using checkerboard tests are contoured by white dashed lines.

vertical fractures and cracks give way to deeper horizontal layering, where the lava flows and/or sub-horizontal intrusions become predominant according to well cuttings (Wu et al., 2024). The single, nearly aseismic, low-scattering anomaly agrees well with their interpretation, as homogeneous volcanic intrusions are thought to lead to a reduction in reverberating and trapped waves and, thus, to a decrease in scattering (King, De Siena, Benson, & Vinciguerra, 2023; King, De Siena, Zhang, et al., 2023).

It should be noted that due to the study area selection, and consequently the earthquakes selected for the analysis, we have low resolution in the high-scattering Húsmúli injection zone (Hù), located between the Hellisheidi power plant and the central Hengill volcano (Slice AA' in Figure 4). Húsmúli is characterized by intense seismic activity (cluster H1 in Obermann et al., 2022), mainly related to fluid reinjection in pre-existing faults, which supports the high seismic scattering observed. Being at the limit of the scattering resolution (Figures S2 in Supporting

21699356, 2025, 5, Downloaded from https://agupubs.onlinelibrary.wiley.com/doi/10.1029/2024JB030731 by CochraneItalia, Wiley Online Library on [09/05/2025]. See the Terms and Conditions (https://onlinelibrary.wiley.com/terms-and-conditions) on Wiley Online Library for rules of use; OA articles are governed by the applicable Creative Commons License

Information S1), we refrain from interpreting the scattering estimates in this region. Importantly, our analysis also does not cover the main production area of the Hellisheiði power plant, Skarðsmýrarfjall and Hverahlíð, located further south of the investigated area.

4.2. Nesjavellir Geothermal Field (Ne)

The volume under the Nesjavellir geothermal area (Ne in Figure 2) has good resolution for both scattering (hit count in Figure S2 in Supporting Information S1) and absorption (checkerboard tests in Figure S4 in Supporting Information S1). This allows us to provide an interpretation of the high-scattering anomaly characterizing volumes right below the Nesjavellir production area between depths of 1 and 6.5 km (Figures 2–4), and of the only high-absorption anomaly detected in this area.

High scattering anomalies at shallow depths (<2.5 km) are coincident in space with both natural- and production-induced microseismicity (Obermann et al., 2022), while at greater depths (>2.5 km) the natural seismicity is predominant (Amoroso et al., 2022; Obermann et al., 2022). Shallow high-scattering values can be explained by strong heterogeneities due to a large number of small faults (in the order of hundreds of meters) and fractures that characterize the area, as observed across rifts (Reiss et al., 2022) and in the highly fractured and tectonically complex continental crust (Napolitano et al., 2020). The scattering images suggest that strong heterogeneities, consistent with a highly complex fault system, are co-located with the deeper, NE-SW-trending, natural seismicity that is aligned with the fissure swarm. With increasing complexity the relative scattering value increases, compared with the overall Hengill region. The almost vertical low-to-high scattering contrast observed immediately to the west of the Nesjavellir production area (Slice BB' in Figure 4) delineates an abrupt change between a highly fractured volume to the east and a more coherent crust to the west. The hit count map (Figure S2 in Supporting Information S1) allows us to interpret this scattering contrast from the surface down to a depth of 4 km, below which, as also evident from the smearing effect at a depth of 5.5 km (Slice BB' in Figure 4), the scattering map is not well recovered. The highly fractured block coincides in space with the harnessed geothermal system and is consistent with the fracture-dominated flow observed. Based on recent scattering results in tectonic environments (Gabrielli et al., 2023; Napolitano et al., 2023; Nardoni & Persaud, 2024), we also infer that this strong lateral scattering contrast might likely depict a quasi-vertical fault structure, belonging to the Hengill fissure swarms as suggested by Wu et al. (2024). The absence of seismic events along this possible fault structure between 2017 and 2022 indicates that it was inactive during the study period. In the nearby Reykjanes peninsula, recent observations of extreme fracture generation during intrusive volcanic events suggest that the fracturing in fissure swarms along extensional boundaries may occur principally in highly active periods during volcanic unrest (Sigmundsson et al., 2024).

The strongest absorption anomaly in the Nesjavellir geothermal field is observed at 4–6.5 km depth, below what is considered the geothermal reservoir in the area, already marked by high-scattering, and at the southern edge of the deep earthquake cluster of natural seismicity. In contrast, low-to-average absorption values are observed at shallower depths (Figure 4). The high-absorption anomaly coincides spatially with a high-Vp/Vs anomaly (>1.9, from Amoroso et al., 2022) found at the same depth (Figure 3). They found the high Vp/Vs anomaly likely to represent the Nesjavellir geothermal heat source, as it correlated spatially with the shallow and deep up-doming of low resistivity layers and the highest well temperatures. It is therefore likely that the strong absorption anomaly is also related to the heat source of the Nesjavellir geothermal system. Slice BB' in Figure 4 shows that the deeper natural seismogenic volume (>3 km depth) beneath the Nesjavellir production area borders the eastern flank of the high-absorption and high-Vp/Vs anomaly. Further investigating this seismicity, we find that part of the deep events are grouped in clusters of events of similar waveforms (green-filled dots in Figure 4). The hottest wells in Nesjavellir (>380°C at 1.5–2.0 km depth, Gunnarsson et al., 2011) are also located right above the high-absorption anomaly.

The interpretation of this high-scattering and high-absorption volume, which has been shown to have high Vp/Vs and low-resistivity, and is bordered to the east by small-magnitude and partially clusterized seismicity, is not straightforward in such a complex region. This is mainly due to the fact that the interpretation of high-attenuation anomalies is non-unique and must be based on geological context and evidence independent of attenuation analysis. In a tectonic environment such as the Apennines mountain chain in Central and Southern Italy, high-absorption bodies revealed in a highly fractured volume suggested the presence of comparable fluid reservoirs (Gabrielli et al., 2022; Napolitano et al., 2023). The presence of fluids filling a complex network of faults and

21699356, 2025, 5, Downloaded from https://agupubs.onlinelibrary.wiley.com/doi/10.1029/2024JB030731 by CochraneItalia, Wiley Online Library on [09/05/2025]. See the Terms and Conditions (https://onlinelibrary.wiley.com/terms-and-conditions) on Wiley Online Library for rules of use; OA articles are governed by the applicable Creative Commons License

fractures, especially in a geothermal environment such as the Nesjavellir geothermal field, is the most straightforward interpretation of this anomaly. However, evidence from the well NJ-11, one of the deepest wells in the region, at the western edge of the Nesjavellir Valley, suggests that more likely the high-attenuation anomaly is caused by excess heat. This well shows a temperature profile that transitions from a boiling point curve shape, indicative of mixing within a geothermal reservoir, to a geothermal gradient, indicative of conductive heat flow, at about 2 km depth (Steingrímsson et al., 1990). This suggests a transition from a more permeable zone above 2 km to a less permeable zone below. Furthermore, the temperatures at the bottom of the well (at 2100 m depth), reached at least 380°C, the maximum range of the thermometer used (Steingrímsson et al., 1990). Finally, the brittle-ductile transition in the area is shallow (6–7 km depth; Tryggvason et al., 2002; Li et al., 2019).

Therefore, we suggest the presence (or co-existence with fluids) of high-absorption melt-filled pore-spaces/fractures. Recent scattering and absorption works performed in volcanic environments support this speculation as they have revealed the sensitivity of seismic absorption to small-scale thermal anomalies related to feeding and eruptive pathways (Guardo et al., 2022; Reiss et al., 2022). At Deception Island (Antarctica), Guardo et al. (2022) observed deep eruptive pathways from the caldera center to its rim with high absorption anomalies. In the Natron Rift (East Africa), more similar to our volcanic context, Reiss et al. (2022) observed both high-scattering and high-absorption anomalies in the top 6 km of the crust, in relation to fluid-filled faults that degas magmatic fluids and high-fractured dyke pathways. They also observed a single high-absorption anomaly within the more ductile part of the crust, interpreted as a melt reservoir that feeds eruptions at Oldoinyo Lengai volcano.

4.3. Non-Harnessed Areas

Across Mosfellsheiði and Ölkelduháls (Mos and Ölk in Figures 2 and 3), two non-harnessed areas within our study region, the event-station distribution and the synthetic tests (Figures S2 and S4 in Supporting Information S1) allow us to interpret most of the results in terms of scattering and absorption. In more detail, scattering maps can be interpreted between 2.2 and 6.5 km depth for Mosfellsheiði, while the Ölkelduháls area is well-resolved between 3.3 and 7.6 km depth (Figure S2 in Supporting Information S1). Absorption anomalies, on the other hand, are well resolved at the depths where they appear, as clearly demonstrated by the checkerboard tests (Figure S4 in Supporting Information S1).

4.3.1. Mosfellsheiði (Mos)

Mosfellsheiði (Mos in Figures 2 and 3) comprises a dormant shield volcano (last eruption >10 kyr) and its lava fields and is located to the west of the Nesjavellir geothermal field (Sæmundsson et al., 2016). The seismicity rate in the area is high and is focused between depths of 3–7 km (Obermann et al., 2022). The underlying mechanisms of the seismicity are unknown, as the area lies outside the Hengill fissure swarm, and there are no geothermal surface manifestations. Horizontal and vertical cross-sections through the scattering model (Figures 2 and 3 and slice CC' in Figure 5) show that the bulk of the seismicity (Obermann et al., 2022) occurred at the interface between high-to-low scattering anomalies. This is most clear at 4.3 km depth (Figure 3), where the northernmost NW-SE-trending seismicity bends southwards, always following the interface between high and low scattering. The seismicity stops at the surface trace of the Hengill central volcano (He in Figure 3), which is dominated by low-scattering at and below 4.3 km depth.

A single high-absorption anomaly is observed at 3.5–5.5 km depth (Figure 5), within the depth range of the earthquakes. The absolute value of the Mosfellsheiði high-absorption anomaly is slightly higher than those found in the Nesjavellir geothermal area at similar depths (Slice BB' in Figure 4 and CC' in Figure 5). This volume correlates spatially with Vp/Vs values reaching 1.8 found by Obermann et al. (2022) at the edge of their well-resolved area. Larger Vp/Vs values (>1.84) have been found 3 km south of our high absorption anomaly at the same depths (Obermann et al., 2022). Although the two anomalies are shifted by a few km, the proximity is indicative of a body with similar characteristics to the high-Vp/Vs and high-absorption volume at the same depth under Nesjavellir (Slice BB' in Figure 4). In addition, Árnason et al. (2010) showed that a deep-lying low-resistivity zone at these depths stretches from the Hengill central volcano toward Mosfellisheiði. Notably, all the earthquakes are located outside the aseismic high-absorption anomaly (Figure 3), surrounding its eastern flank (Figure 5, slice CC'). The absorption inversion procedure does not invert for seismic event locations, which have been computed independently and merely superimposed on the absorption maps, thereby increasing the significance of these findings (see Section 3). The results also revealed that the seismicity partially occurred as clusters

21699356, 2025, 5, Downloaded from https://agupubs.onlinelibrary.wiley.com/doi/10.1029/2024JB030731 by CochraneItalia, Wiley Online Library on [09/05/2025]. See the Terms and Conditions (https://onlinelibrary.wiley.com/terms-and-conditions) on Wiley Online Library for rules of use; OA articles are governed by the applicable Creative Commons License

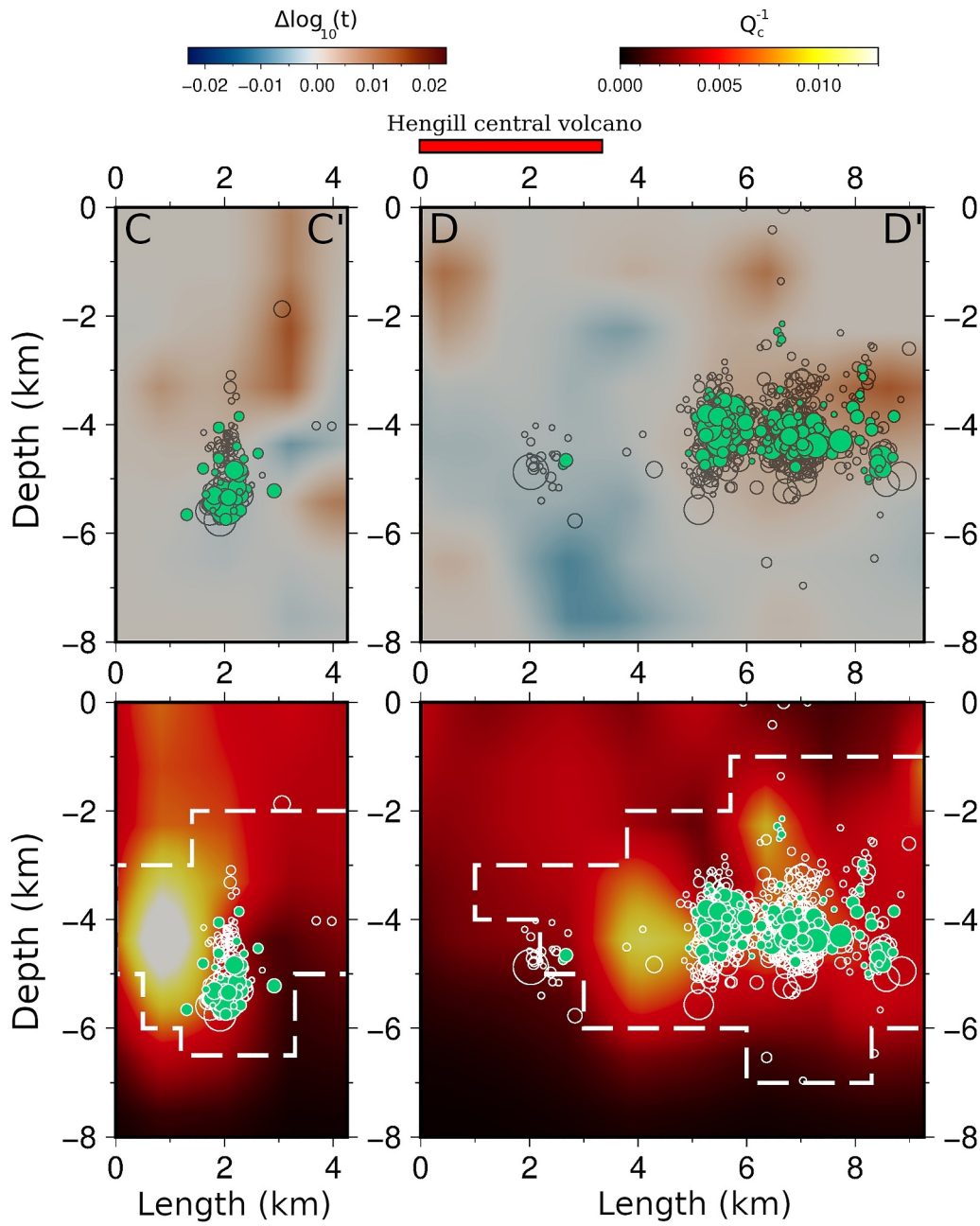

Figure 5. Cross-sections CC' (showing Mosfellsheiði) and DD' (crossing Hengill central volcano and Ölkelduháls, see Figure 1b for reference) showing scattering (upper panels) and absorption (lower panels) results. Gray and white circles show the earthquakes within 500 m from each cross-section. The green circles belong to clusters of events producing similar waveforms. Well-resolved absorption volumes are contoured by white dashed lines.

of events of similar waveforms (normalized cross-correlation, CC > 0.7, Slices CC' in Figure 5). Wu et al. (2024) used Voigt average isotropic S velocity ($v_{\text{voigt}} = \sqrt{(2V_{SV}^2 + V_{SH}^2)/3}$, where V_{SV} and v_{SH} are the S-wave vertical and horizontal velocity components, respectively) and anisotropic ambient noise imaging, finding that the first 2 km in this area were characterized by very low V_{voigt} (<1.7 km/s). At greater depths, a high V_{voigt} (>3.8 km/s) coincides instead with the high-absorption volume. Wu et al. (2024) suggest that mineral alteration that yields clay formation is the likeliest reason for the anomalously low shear wave velocity. Still, the nature of the deep

21699356, 2025, 5, Downloaded from https://agupubs.onlinelibrary.wiley.com/doi/10.1029/2024JB030731 by CochraneItalia, Wiley Online Library on [09/05/2025]. See the Terms and Conditions (https://onlinelibrary.wiley.com/terms-and-conditions) on Wiley Online Library for rules of use; OA articles are governed by the applicable Creative Commons License

high-velocity anomaly remains unknown. Low-velocities (<1.5 km/s) in the shallower crust of Mosfellsheiði were also found by Sanchez-Pastor et al. (2021) down to a depth of 3 km.

Our results, jointly interpreted with those from previous and independent studies, suggest the high-scattering and high-absorption body likely reveals the presence of a fluid- and/or melt-filled fault network at depths of 3.5–5.5 km. In analogy with the volume under the Nesjavellir geothermal field, the high Vp/Vs, high absorption and low-resistivity volume likely play a pivotal role in the triggering of earthquake swarms occurring in the short time span of 2018–2021. A more in-depth analysis of the seismicity could give more insights into the triggering mechanism of these clusters. The Mosfellsheiði area is unharnessed and consequently lacks well data and, therefore, in situ lithological and temperature measurements. The scattering and absorption anomalies suggest that this could be an interesting site for geothermal development, with a rich geo-resource at a depth comparable with that in the Nesjavellir geothermal field, despite the absence of surface geothermal manifestations.

4.3.2. Ölkelduháls (Ölk)

Ölkelduháls (Ölk in Figures 2 and 3) lies southeast of Hengill, northwest of Grensdalur, and southwest of Hrómundartindur central volcanoes. In Ölkelduháls, the natural seismicity is concentrated between depths of 1 and 6 km and characterized by a moderate earthquake rate (Obermann et al., 2022). The continuous WNW-ESE-striking seismicity between depths of 3–5 km occurs mainly in areas marked by high scattering (Figures 2, 3 and 5), and is spatially confined among the three central volcanoes, disappearing at the interface with the deep low-scattering structure of Hengill (Slice DD' in Figure 5).

Two high-absorption anomalies appear at depths of 3.5 and 5.5 km between Hengill and Grensdalur (Figure 3 and slice DD' in Figure 5). A third high-absorption anomaly is located further east, between Grensdalur and Hrómundartindur, at the limit of the model resolution and thus is not interpreted. The absolute values of these anomalies are comparable with those in Nesjavellir (Figure 3). Of the two anomalies, the one further southeast (the closest to Grensdalur) is smaller, shallower (up to a depth of about 2.2 km) and vertically oriented. A vertically oriented high-absorption anomaly has been retrieved under Mt. Pollino in Italy. Napolitano et al. (2023) interpreted it as the signature of fluids migrating toward known faults during a long-lasting seismic sequence and feeding surface deep-sourced springs. How significant this anomaly is in the Ölkelduháls case study is unclear, due to the lack of studies about fault structures that could corroborate this inference.

The spatial distribution of the seismicity at Ölkelduháls has been related to an up-doming low-V_{VOIGT} body (slow S-waves) at depths greater than 3 km and interpreted as evidence of a shallow brittle-ductile-transition zone (Wu et al., 2024). In addition, the Ölkelduháls area hosted the 2006–2017 subsidence (white hexagon Figure 3) (Juncu et al., 2017) and a subsequent uplift episode (2017–2018) located 3 km NNW of an uplift episode that occurred between 1993 and 1999 (green hexagon Figure 3). The latter occurred at a depth of approximately 5–7 km (Ducrocq et al., 2021; Feigl et al., 2000), located close to the brittle-ductile transition (Li et al., 2019). Part of these events are also included in our data sets, and clusters of similar waveforms have been found among these earthquakes (Slice DD' in Figure 5). The nature of these processes is debated. It been proposed to be hydrothermal or magmatic (Ducrocq et al., 2021). The seismic tomography study from Tryggvason et al. (2002), targeting the 1993–1999 inflation beneath SW Hrómundartindur, finds seismic velocities at these depths to be more consistent with those of rocks where pore space is filled with supercritical fluids, rather than those of melt bodies. The permeability in the Ölkelduháls reservoir is relatively high. High flow rates were observed in the two deep wells there located. Geothermal surface manifestations are much greater than in Nesjavellir (Figure 1). Similar high-absorption and high-attenuation anomalies have been detected at the location of sources of ground deformation both of hydrothermal (like at Campi Flegrei, De Siena et al., 2017) and magmatic (Ol Doyinio Lengai, Reiss et al., 2022) nature. In the Ölkelduháls area, the deeper (>3 km), high-absorption anomaly (Figures 3 and 5) coincides spatially with the modeled source of the observed surface deformation (within uncertainty). The depth, characteristics and spatial correlation of the high-absorption anomaly with the high Vp/Vs of Jousset et al. (2011) and low resistivity values at the same depths (Árnason et al., 2010) suggest that they are more likely due to geothermal fluids trapped within the crust than melt. The upward flow of these fluids occurs through a highly fractured high-scattering medium in small, vertically oriented structures as suggested by independent anisotropy analyses (Wu et al., 2024), resulting in hot springs and extensive geothermal manifestations.

21699356, 2025, 5, Downloaded from https://agupubs.onlinelibrary.wiley.com/doi/10.1029/2024JB030731 by CochraneItalia, Wiley Online Library on [09/05/2025]. See the Terms and Conditions (https://onlinelibrary.wiley.com/terms-and-conditions) on Wiley Online Library for rules of use; OA articles are governed by the applicable Creative Commons License

5. Conclusion

Seismic scattering and absorption are more sensitive to variations in rheology, fracturing levels and fluid and/or melt content within the crust than seismic wave velocities. They, therefore, have the potential to be key parameters for identifying and delineating geothermal resources. Here, we present the first 3D scattering and absorption imaging of the Hengill region (SW Iceland) obtained using the peak delay and Q-coda methodology. The results allow interpretation of crustal structures under the Hengill central volcano, the Nesjavellir geothermal field and two non-harnessed areas: Mosfellsheiði, located to the west of Nesjavellir, and Ölkelduháls, located in-between the three central volcanoes (Hengill, Grensdalur and Hrómundartindur).

Within the Hengill central volcano, a shallow SW-NE-trending high-scattering anomaly marks the fissure swarm. High-to-low scattering contrasts on the west and east sides of Hengill (reflecting the shape of the central volcano) are interpreted as the transition from a more fractured crust within the fissure zone of Hengill to a more coherent crust on either side of the volcano. At depths greater than 3 km, a wide low-scattering anomaly reflects a change from shallow sub-vertical fractures and cracks to predominant sub-horizontal intrusions that reduce wave reverberation and consequently decrease seismic scattering. Outside the Hengill central volcano, scattering is usually high, highlighting strong heterogeneity, within which mostly natural but also induced (from geothermal operations) small-magnitude earthquakes occur.

In the Nesjavellir geothermal field, a high-scattering and high-absorption volume coincides with the high-Vp/Vs and low-resistivity anomaly previously found at around 4.5 km depth in the production area of the Nesjavellir power plant, where the hottest production wells are located. These volumes are interpreted as fluid-filled complex networks of faults and fractures. However, we cannot exclude the presence (or co-existence with fluids) of melt-filled fractures within this volume.

We also imaged scattering and absorption across two neighboring non-harnessed areas: Mosfellsheiði and Ölkelduháls. In both areas co-located high-absorption and high-scattering volumes mark the likely presence of fluid and/or melt reservoirs at depths comparable to those found in Nesjavellir. In the case of Mosfellsheiði, the lack of well data and, therefore, in situ lithological and temperature measurements do not provide further corroborations of our results. On the contrary, in Ölkelduháls, our interpretation is supported by surface geothermal manifestation, uplift and subsidence episodes, strong groundwater flux, and clusters of events of similar waveforms.

In conclusion, the analysis demonstrates the potential of scattering and absorption imaging as new complementary tools to existing geophysical methods for geothermal resource exploration. Our analysis suggests that the geothermal development should focus in Mosfellsheiði area despite the absence of geothermal surface manifestations.

Data Availability Statement

Seismic networks used in this study are: 2C, OR and VI (http://www.coseismiq.ethz.ch/en/dissemination/stations/). All stations are discoverable using fdsnws:stations, for example, http://eida-federator.ethz.ch/fdsnws/station/1/query?net=2C,OR,VI&format=text&level=station&nodata=404. Seismic waveforms are stored and openly available on the European Integrated Data Archive (EIDA). An example of how to download data in the analyzed period for the used seismic network is: https://eida.ethz.ch/fdsnws/dataselect/1/query?network=OR&network=2C&network=VI&starttime=2017-01-01T00:00:00&endtime=2022-12-31T00:00:00. The seismic catalog used in this analysis is available at Zenodo repository (Reykjavík Energy, 2024). The software Murat3.0, the third release of an open-access code (De Siena et al., 2014), used to perform scattering and absorption imaging of this area is available at Zenodo repository (Napolitano, 2024). Figures 1 and 2 have been obtained through the GMT 6 (Wessel et al., 2019), accessible and downloadable at https://www.generic-mapping-tools.org/download/. Figures 4 and 5 have been obtained through GMT 6 and Paraview software version 5.11.1 (Ahrens et al., 2005), available under BSD 3-Clause license at https://www.paraview.org/resources/. Colormaps have been created using the Scientific color maps (Crameri et al., 2020) accessible from the following link: https://www.fabiocrameri.ch/colourmaps/ and also stored on Zenodo (Crameri, 2023).

21699356, 2025, 5, Downloaded from https://agupubs.onlinelibrary.wiley.com/doi/10.1029/2024JB030731 by CochraneItalia, Wiley Online Library on [09/05/2025]. See the Terms and Conditions (https://onlinelibrary.wiley.com/terms-and-conditions) on Wiley Online Library for rules of use; OA articles are governed by the applicable Creative Commons License

Acknowledgments
We thank the Geothermica ERA-net funded COSEISMIQ project (project 170167-4401) for data from six of their stations, and Icelandic Meteorological Office (IMO) for data from one station. We thank ÍSOR and ON Power for the use of their extensive data set on manually refined phase-picks. We are thankful to Thomas Hudson and the anonymous reviewer, whose comments significantly improved the quality of the manuscript. This work has been partially supported by the S4CE ("Science for Clean Energy") project, funded by the European Union's Horizon 2020—R&I Framework Programme, under Grant agreement 764810. F.N. was partially funded by the project TOGETHER - Sustainable geothermal energy for two Southern Italy regions: geophysical resource evaluation and public awareness financed by European Union—Next Generation EU Piano Nazionale di Ripresa (PNRR) e Resilienza Missione 4 "Istruzione e Ricerca" - Componente C2, Investimento 1.1, "Fondo per il Programma Nazionale di Ricerca e Progetti di Rilevante Interesse Nazionale (PRIN)" CUP: D53D23022850001, project code: P2022JF5JE. Open access publishing facilitated by Universita degli Studi di Salerno, as part of the Wiley - CRUI-CARE agreement.

References

Ahrens, J., Geveci, B., Law, C., Hansen, C., & Johnson, C. (2005). 36-paraview: An end-user tool for large-data visualization. *The visualization handbook*, *717*, 50038–50041. https://doi.org/10.1016/B978-012387582-2/50038-1

Akande, W. G., De Siena, L., & Gan, Q. (2019). Three-dimensional kernel-based coda attenuation imaging of caldera structures controlling the 1982-84 Campi Flegrei unrest. *Journal of Volcanology and Geothermal Research*, *381*, 273–283. https://doi.org/10.1016/j.jvolgeores.2019.06.007

Aki, K., & Chouet, B. (1975). Origin of coda waves: Source, attenuation, and scattering effects. *Journal of Geophysical Research*, *80*(23), 3322–3342. https://doi.org/10.1029/JB080i023p03322

Amoroso, O., Napolitano, F., Hersir, G. P., Agustsdottir, T., Convertito, V., De Matteis, R., et al. (2022). 3D seismic imaging of the Nesjavellir geothermal field, SW-Iceland. *Frontiers in Earth Science*, *10*, 994280. https://doi.org/10.3389/feart.2022.994280

Árnason, K., Eysteinsson, H., & Hersir, G. P. (2010). Joint 1D inversion of TEM and MT data and 3D inversion of MT data in the Hengill area, SW Iceland. *Geothermics*, *39*(1), 13–34. https://doi.org/10.1016/j.geothermics.2010.01.002

Árnason, K., Haraldsson, G. I., Johnsen, G. V., Thorbergsson, G., Hersir, G. P., Saemundsson, K., et al. (1986). Nesjavellir. Geological and geophysical surveys in 1985 Orkustofnun report. *Icelandic*, *125*.

Block, L. V. (1991). *Joint hypocenter-velocity inversion of local earthquake arrival time data in two geothermal regions*. Doctoral dissertation, Massachusetts Institute of Technology.

Bodvarsson, R., Rognvaldsson, S. T., Jakobsdottir, S. S., Slunga, R., & Stefansson, R. (1996). The SIL data acquisition and monitoring system. *Seismological Research Letters*, *67*(5), 35–46. https://doi.org/10.1785/gssrl.67.5.35

Borleanu, F., De Siena, L., Thomas, C., Popa, M., & Radulian, M. (2017). Seismic scattering and absorption mapping from intermediate-depth earthquakes reveals complex tectonic interactions acting in the Vrancea region and surroundings (Romania). *Tectonophysics*, *706*, 129–142. https://doi.org/10.1016/j.tecto.2017.04.013

Brandsdóttir, B., Parsons, M., White, R. S., Guðmundsson, O., Drew, J., & Thorbjarnadóttir, B. (2010). The May 29 2008 earthquake aftershock sequence within the South Iceland Seismic Zone: Fault locations and source parameters of aftershocks. *Jökull Journal: journal of the glaciological and geological societies of Iceland*, *60*, 23–46.

Calvet, M., & Margerin, L. (2013). Lapse-time dependence of coda Q: Anisotropic multiple-scattering models and application to the Pyrenees. *Bulletin of the Seismological Society of America*, *103*(3), 1993–2010. https://doi.org/10.1785/0120120239

Calvet, M., Sylvander, M., Margerin, L., & Villaseñor, A. (2013). Spatial variations of seismic attenuation and heterogeneity in the Pyrenees: Coda Q and peak delay time analysis. *Tectonophysics*, *608*, 428–439. https://doi.org/10.1016/j.tecto.2013.08.045

Crameri, F. (2023). Scientific colour maps (8.0.1). *Software] Zenodo*. https://doi.org/10.5281/zenodo.8409685

Crameri, F., Shephard, G. E., & Heron, P. J. (2020). The misuse of colour in science communication. *Nature Communications*, *11*(1), 5444. https://doi.org/10.1038/s41467-020-19160-7

Danré, P., De Barros, L., Cappa, F., & Ampuero, J. P. (2022). Prevalence of aseismic slip linking fluid injection to natural and anthropogenic seismic swarms. *Journal of Geophysical Research: Solid Earth*, *127*(12), e2022JB025571. https://doi.org/10.1029/2022JB025571

De Barros, L., Cappa, F., Deschamps, A., & Dublanchet, P. (2020). Imbricated aseismic slip and fluid diffusion drive a seismic swarm in the Corinth Gulf, Greece. *Geophysical Research Letters*, *47*(9), e2020GL087142. https://doi.org/10.1029/2020GL087142

Del Pezzo, E., De La Torre, A., Bianco, F., Ibanez, J., Gabrielli, S., & De Siena, L. (2018). Numerically calculated 3D space-weighting functions to image crustal volcanic structures using diffuse coda waves. *Geosciences*, *8*(5), 175. https://doi.org/10.3390/geosciences8050175

De Matteis, R., Convertito, V., Napolitano, F., Amoroso, O., Terakawa, T., & Capuano, P. (2021). Pore fluid pressure imaging of the Mt. Pollino region (southern Italy) from earthquake focal mechanisms. *Geophysical Research Letters*, *48*(22), e2021GL094552. https://doi.org/10.1029/2021GL094552

De Siena, L., Calvet, M., Watson, K. J., Jonkers, A. R. T., & Thomas, C. (2016). Seismic scattering and absorption mapping of debris flows, feeding paths, and tectonic units at Mount St. Helens volcano. *Earth and Planetary Science Letters*, *442*, 21–31. https://doi.org/10.1016/j.epsl.2016.02.026

De Siena, L., Chiodini, G., Vilardo, G., Del Pezzo, E., Castellano, M., Colombelli, S., et al. (2017). Source and dynamics of a volcanic caldera unrest: Campi Flegrei, 1983–84. *Scientific Reports*, *7*(1), 8099. https://doi.org/10.1038/s41598-017-08192-7

De Siena, L., Del Pezzo, E., Thomas, C., Curtis, A., & Margerin, L. (2013). Seismic energy envelopes in volcanic media: In need of boundary conditions. *Geophysical Journal International*, *195*(2), 1102–1119. https://doi.org/10.1093/gji/ggt273

De Siena, L., Thomas, C., Waite, G. P., Moran, S. C., & Klemme, S. (2014). Attenuation and scattering tomography of the deep plumbing system of Mount St. Helens. *Journal of Geophysical Research: Solid Earth*, *119*(11), 8223–8238. https://doi.org/10.1002/2014JB011372

Di Martino, M. D. P., De Siena, L., Serlenga, V., & De Landro, G. (2022). Reconstructing hydrothermal fluid pathways and storage at the Solfatara Crater (Campi Flegrei, Italy) using seismic scattering and absorption. *Frontiers in Earth Science*, *10*, 852510. https://doi.org/10.3389/feart.2022.852510

Di Martino, M. D. P., De Siena, L., & Tisato, N. (2022). Pore space topology controls ultrasonic waveforms in dry volcanic rocks. *Geophysical Research Letters*, *49*(18), e2022GL100310. https://doi.org/10.1029/2022GL100310

Ducrocq, C., Geirsson, H., Árnadóttir, T., Juncu, D., Drouin, V., Gunnarsson, G., et al. (2021). Inflation-deflation episodes in the Hengill and Hrómundartindur volcanic complexes, SW Iceland. *Frontiers in Earth Science*, *9*, 725109. https://doi.org/10.3389/feart.2021.725109

Einarsson, P. (2008). Plate boundaries, rifts and transforms in Iceland. *Jökull Journal*, *58*(12), 35–58. https://doi.org/10.33799/jokull2008.58.035

Feigl, K. L., Gasperi, J., Sigmundsson, F., & Rigo, A. (2000). Crustal deformation near Hengill volcano, Iceland 1993–1998: Coupling between magmatic activity and faulting inferred from elastic modeling of satellite radar interferograms. *Journal of Geophysical Research*, *105*(B11), 25655–25670. https://doi.org/10.1029/2000JB900209

Fischer, T., Horálek, J., Hrubcová, P., Vavryčuk, V., Bräuer, K., & Kämpf, H. (2014). Intra-continental earthquake swarms in West-Bohemia and Vogtland: A review. *Tectonophysics*, *611*, 1–27. https://doi.org/10.1016/j.tecto.2013.11.001

Foulger, G. R., & Toomey, D. R. (1989). Structure and evolution of the Hengill-Grensdalur volcanic complex, Iceland: Geology, geophysics, and seismic tomography. *Journal of Geophysical Research*, *94*(B12), 17511–17522. https://doi.org/10.1029/JB094iB12p17511

Franzson, H., Gunnlaugsson, E., Árnason, K., Sæmundsson, K., Steingrímsson, B., & Hardarson, B. S. (2010). The Hengill geothermal system, conceptual model and thermal evolution. *Proceedings World Geothermal Congress*, *25*, 1.

Gabrielli, S., Akinci, A., De Siena, L., Del Pezzo, E., Buttinelli, M., Maesano, F. E., & Maffucci, R. (2023). Scattering attenuation images of the control of thrusts and fluid overpressure on the 2016–2017 Central Italy seismic sequence. *Geophysical Research Letters*, *50*(8), e2023GL103132. https://doi.org/10.1029/2023GL103132

21699356, 2025, 5, Downloaded from https://agupubs.onlinelibrary.wiley.com/doi/10.1029/2024JB030731 by CochraneItalia, Wiley Online Library on [09/05/2025]. See the Terms and Conditions (https://onlinelibrary.wiley.com/terms-and-conditions) on Wiley Online Library for rules of use; OA articles are governed by the applicable Creative Commons License

Gabrielli, S., Akinci, A., Ventura, G., Napolitano, F., Del Pezzo, E., & De Siena, L. (2022). Fast changes in seismic attenuation of the upper crust due to fracturing and fluid migration: The 2016–2017 central Italy seismic sequence. *Frontiers in Earth Science*, *10*, 909698. https://doi.org/10.3389/feart.2022.909698

Gabrielli, S., De Siena, L., Napolitano, F., & Del Pezzo, E. (2020). Understanding seismic path biases and magmatic activity at Mount St Helens volcano before its 2004 eruption. *Geophysical Journal International*, *222*(1), 169–188. https://doi.org/10.1093/gji/ggaa154

Guardo, R., De Siena, L., Prudencio, J., & Ventura, G. (2022). Imaging the absorbing feeding and eruptive pathways of Deception Island, Antarctica. *Geophysical Research Letters*, *49*(19), e2022GL099540. https://doi.org/10.1029/2022GL099540

Gunnarsson, G., & Aradóttir, E. S. (2015). The deep roots of geothermal systems in volcanic areas: Boundary conditions and heat sources in reservoir modeling. *Transport in Porous Media*, *108*(1), 43–59. https://doi.org/10.1007/s11242-014-0328-1

Gunnarsson, G., Arnaldsson, A., & Oddsdóttir, A. L. (2011). Model simulations of the Hengill area, southwestern Iceland. *Transport in Porous Media*, *90*(1), 3–22. https://doi.org/10.1007/s11242-010-9629-1

Gusev, A. A., & Abubakirov, I. R. (1999). Vertical profile of effective turbidity reconstructed from broadening of incoherent body-wave pulses—I. General approach and the inversion procedure. *Geophysical Journal International*, *136*(2), 295–308. https://doi.org/10.1046/j.1365-246X.1999.00740.x

Jakobsdóttir, S. S. (2008). Seismicity in Iceland: 1994–2007. *Jökull Journal*, *58*(1), 75–100. https://doi.org/10.33799/jokull2008.58.075

Jousset, P., Haberland, C., Bauer, K., & Arnason, K. (2011). Hengill geothermal volcanic complex (Iceland) characterized by integrated geophysical observations. *Geothermics*, *40*(1), 1–24. https://doi.org/10.1016/j.geothermics.2010.12.008

Juncu, D., Árnadóttir, T., Hooper, A., & Gunnarsson, G. (2017). Anthropogenic and natural ground deformation in the Hengill geothermal area, Iceland. *Journal of Geophysical Research: Solid Earth*, *122*(1), 692–709. https://doi.org/10.1002/2016JB013626

King, T., De Siena, L., Benson, P., & Vinciguerra, S. (2023). Mapping faults in the laboratory with seismic scattering 1: The laboratory perspective. *Geophysical Journal International*, *232*(3), 1590–1599. https://doi.org/10.1093/gji/ggac409

King, T., De Siena, L., Zhang, Y., Nakata, N., Benson, P., & Vinciguerra, S. (2023). Mapping faults in the laboratory with seismic scattering 2: The modelling perspective. *Geophysical Journal International*, *234*(2), 1024–1031. https://doi.org/10.1093/gji/ggad100

Li, K. L., Abril, C., Gudmundsson, O., & Gudmundsson, G. B. (2019). Seismicity of the Hengill area, SW Iceland: Details revealed by catalog relocation and collapsing. *Journal of Volcanology and Geothermal Research*, *376*, 15–26. https://doi.org/10.1016/j.jvolgeores.2019.03.008

Margerin, L. (2017). Breakdown of equipartition in diffuse fields caused by energy leakage. *The European Physical Journal Special Topics*, *226*(7), 1353–1370. https://doi.org/10.1140/epjst/e2016-60165-6

Mayor, J., Calvet, M., Margerin, L., Vanderhaeghe, O., & Traversa, P. (2016). Crustal structure of the Alps as seen by attenuation tomography. *Earth and Planetary Science Letters*, *439*, 71–80. https://doi.org/10.1016/j.epsl.2016.01.025

Napolitano, F. (2024). ferdinandonapolitano/Attenuation_Hengill: (v. 1). *Zenodo*. [Software]. https://doi.org/10.5281/zenodo.14001492

Napolitano, F., De Siena, L., Gervasi, A., Guerra, I., Scarpa, R., & La Rocca, M. (2020). Scattering and absorption imaging of a highly fractured fluid-filled seismogenetic volume in a region of slow deformation. *Geoscience Frontiers*, *11*(3), 989–998. https://doi.org/10.1016/j.gsf.2019.09.014

Napolitano, F., Gabrielli, S., De Siena, L., Amoroso, O., & Capuano, P. (2023). Imaging overpressurised fracture networks and geological barriers hindering fluid migrations across a slow-deformation seismic gap. *Scientific Reports*, *13*(1), 19680. https://doi.org/10.1038/s41598-023-47104-w

Napolitano, F., Galluzzo, D., Gervasi, A., Scarpa, R., & La Rocca, M. (2021). Fault imaging at Mt Pollino (Italy) from relative location of microearthquakes. *Geophysical Journal International*, *224*(1), 637–648. https://doi.org/10.1093/gji/ggaa407

Nardoni, C., & Persaud, P. (2024). Evidence for faulting and fluid-driven earthquake processes from seismic attenuation variations beneath metropolitan Los Angeles. *Scientific Reports*, *14*(1), 17595. https://doi.org/10.1038/s41598-024-67872-3

Obermann, A., Planès, T., Larose, E., Sens-Schönfelder, C., & Campillo, M. (2013). Depth sensitivity of seismic coda waves to velocity perturbations in an elastic heterogeneous medium. *Geophysical Journal International*, *194*(1), 372–382. https://doi.org/10.1093/gji/ggt043

Obermann, A., Wu, S. M., Ágústsdóttir, T., Duran, A., Diehl, T., Sánchez-Pastor, P., et al. (2022). Seismicity and 3-D body-wave velocity models across the Hengill geothermal area, SW Iceland. *Frontiers in Earth Science*, *10*, 969836. https://doi.org/10.3389/feart.2022.969836

Ogiso, M. (2019). A method for mapping intrinsic attenuation factors and scattering coefficients of S waves in 3-D space and its application in southwestern Japan. *Geophysical Journal International*, *216*(2), 948–957. https://doi.org/10.1093/gji/ggy468

Paasschens, J. C. J. (1997). Solution of the time-dependent Boltzmann equation. *Physical Review E*, *56*(1), 1135–1141. https://doi.org/10.1103/PhysRevE.56.1135

Palo, M., Ogliari, E., & Sakwa, M. (2024). Spatial pattern of the seismicity induced by geothermal operations at the Geysers (California) inferred by unsupervised machine learning. *IEEE Transactions on Geoscience and Remote Sensing*, *62*, 1–13. https://doi.org/10.1109/TGRS.2024.3361169

Palo, M., Picozzi, M., De Landro, G., & Zollo, A. (2023). Microseismicity clustering and mechanic properties reveal fault segmentation in southern Italy. *Tectonophysics*, *856*, 229849. https://doi.org/10.1016/j.tecto.2023.229849

Palo, M., Scotto di Uccio, F., Picozzi, M., & Festa, G. (2024). An enhanced catalog of repeating earthquakes on the 1980 Irpinia fault system, southern Italy. *Geosciences*, *14*(1), 8. https://doi.org/10.3390/geosciences14010008

Prudencio, J., Aoki, Y., Takeo, M., Ibáñez, J. M., Del Pezzo, E., & Song, W. (2017). Separation of scattering and intrinsic attenuation at Asama volcano (Japan): Evidence of high volcanic structural contrasts. *Journal of Volcanology and Geothermal Research*, *333*, 96–103. https://doi.org/10.1016/j.jvolgeores.2017.01.014

Reiss, M. C., De Siena, L., & Muirhead, J. D. (2022). The interconnected magmatic plumbing system of the Natron Rift. *Geophysical Research Letters*, *49*(15), e2022GL098922. https://doi.org/10.1029/2022GL098922

Reykjavík Energy (Iceland). (2024). Seismic catalog for Hengill 2017-2022: Handpicked earthquakes (1.0). *Zenodo*. [Dataset]. https://doi.org/10.5281/zenodo.14050112

Rögnvaldsson, S. T., Gudmundsson, G., Ágústsson, K., Stefánsson, R., Jakobsdóttir, S., & Thorkelson, B. (1996). Recent seismicity near the Hengill triple-junction, SW Iceland. *Seismology in Europe*, 461–466.

Ross, Z. E., Cochran, E. S., Trugman, D. T., & Smith, J. D. (2020). 3D fault architecture controls the dynamism of earthquake swarms. *Science*, *368*(6497), 1357–1361. https://doi.org/10.1126/science.abb0779

Ruhl, C. J., Abercrombie, R. E., Smith, K. D., & Zaliapin, I. (2016). Complex spatiotemporal evolution of the 2008 Mw 4.9 Mogul earthquake swarm (Reno, Nevada): Interplay of fluid and faulting. *Journal of Geophysical Research: Solid Earth*, *121*(11), 8196–8216. https://doi.org/10.1002/2016JB013399

Sæmundsson, K., Sigurgeirsson, M. Á., Hjartarson, Á., Kaldal, I., Kristinsson, S. G., & Víkingsson, S. (2016). Geological map of SW Iceland, 1: 100 000 (2. edition). *Reykjavík: Iceland GeoSurvey*.

21699356, 2025, 5, Downloaded from https://agupubs.onlinelibrary.wiley.com/doi/10.1029/2024JB030731 by CochraneItalia, Wiley Online Library on [09/05/2025]. See the Terms and Conditions (https://onlinelibrary.wiley.com/terms-and-conditions) on Wiley Online Library for rules of use; OA articles are governed by the applicable Creative Commons License

Sánchez-Pastor, P., Obermann, A., Reinsch, T., Ágústsdóttir, T., Gunnarsson, G., Tómasdóttir, S., et al. (2021). Imaging high-temperature geothermal reservoirs with ambient seismic noise tomography, a case study of the Hengill geothermal field, SW Iceland. *Geothermics*, *96*, 102207. https://doi.org/10.1016/j.geothermics.2021.102207

Sato, H., Fehler, M. C., & Maeda, T. (2012). *Seismic wave propagation and scattering in the heterogeneous earth* (Vol. 496). Springer.

Shapiro, N. M., Campillo, M., Margerin, L., Singh, S. K., Kostoglodov, V., & Pacheco, J. (2000). The energy partitioning and the diffusive character of the seismic coda. *Bulletin of the Seismological Society of America*, *90*(3), 655–665. https://doi.org/10.1785/0119990021

Sigmundsson, F., Einarsson, P., Rögnvaldsson, S. T., Foulger, G. R., Hodgkinson, K. M., & Thorbergsson, G. (1997). The 1994–1995 seismicity and deformation at the Hengill triple junction, Iceland: Triggering of earthquakes by minor magma injection in a zone of horizontal shear stress. *Journal of Geophysical Research*, *102*(B7), 15151–15161. https://doi.org/10.1029/97JB00892

Sigmundsson, F., Parks, M., Geirsson, H., Hooper, A., Drouin, V., Vogfjörd, K. S., et al. (2024). Fracturing and tectonic stress drive ultrarapid magma flow into dikes. *Science*, *383*(6688), 1228–1235. https://doi.org/10.1126/science.adn2838

Sinton, J., Gronvold, K., & Sæmundsson, K. (2005). Postglacial eruptive history of the western volcanic zone, Iceland. *Geochemistry, Geophysics, Geosystems*, *6*(12), Q12009. https://doi.org/10.1029/2005GC001021

Sketsiou, P., Napolitano, F., Zenonos, A., & De Siena, L. (2020). New insights into seismic absorption imaging. *Physics of the Earth and Planetary Interiors*, *298*, 106337. https://doi.org/10.1016/j.pepi.2019.106337

Steingrimsson, B., Gudmundsson, A., Franzson, H., & Gunnlaugsson, E. (1990). SGP-TR-130 Evidence of a supercritical fluid at depth in the Nesjavellir field. In *Workshop Report* (Vol. 15). Stanford Geothermal Program, Stanford University.

Takahashi, T., Sato, H., Nishimura, T., & Obara, K. (2007). Strong inhomogeneity beneath Quaternary volcanoes revealed from the peak delay analysis of S-wave seismograms of microearthquakes in northeastern Japan. *Geophysical Journal International*, *168*(1), 90–99. https://doi.org/10.1111/j.1365-246X.2006.03197.x

Talone, D., De Siena, L., Lavecchia, G., & de Nardis, R. (2023). The attenuation and scattering signature of fluid reservoirs and tectonic interactions in the central-southern Apennines (Italy). *Geophysical Research Letters*, *50*(22), e2023GL106074. https://doi.org/10.1029/2023GL106074

Tryggvason, A., Rögnvaldsson, S. T., & Flóvenz, O. G. (2002). Three-dimensional imaging of the P-and S-wave velocity structure and earthquake locations beneath Southwest Iceland. *Geophysical Journal International*, *151*(3), 848–866. https://doi.org/10.1046/j.1365-246X.2002.01812.x

Vilhjálmsson, A. M., Benediktsdóttir, Á., & Árnason, K. (2019). Nesjavellir og Þverárdalur Einvíð túlkun viðnámsgagna og þrívíð fyrir Nesjavallasvæðið. ÍSOR report, in Icelandic, ÍSOR-2019/062.

Wegler, U. (2004). Diffusion of seismic waves in a thick layer: Theory and application to Vesuvius volcano. *Journal of Geophysical Research: Solid Earth*, *109*(B7). https://doi.org/10.1029/2004JB003048

Wessel, P., Luis, J. F., Uieda, L. A., Scharroo, R., Wobbe, F., Smith, W. H., & Tian, D. (2019). The generic mapping tools version 6. *Geochemistry, Geophysics, Geosystems*, *20*(11), 5556–5564. https://doi.org/10.1029/2019GC008515

Wu, S. M., Sánchez-Pastor, P., Ágústsdóttir, T., Hersir, G. P., Mordret, A., Hjörleifsdóttir, V., & Obermann, A. (2024). Crustal characterization of the Hengill geothermal fields: Insights from isotropic and anisotropic seismic noise imaging using a 500-node array. *Journal of Geophysical Research: Solid Earth*, *129*(7), e2024JB028915. https://doi.org/10.1029/2024JB028915

21699356, 2025, 5, Downloaded from https://agupubs.onlinelibrary.wiley.com/doi/10.1029/2024JB030731 by CochraneItalia, Wiley Online Library on [09/05/2025]. See the Terms and Conditions (https://onlinelibrary.wiley.com/terms-and-conditions) on Wiley Online Library for rules of use; OA articles are governed by the applicable Creative Commons License